

IMAGE SUBTRACTION REDUCTION OF OPEN CLUSTERS M35 & NGC 2158 IN THE *K2* CAMPAIGN-0
SUPER-STAMPM. SOARES-FURTADO^{1,†}, J. D. HARTMAN¹, G. Á. BAKOS^{1,*,**}, C. X. HUANG², K. PENEV¹, W. BHATTI¹

Draft version March 2, 2017

ABSTRACT

Observations were made of the open clusters M35 and NGC 2158 during the initial *K2* campaign (C0). Reducing these data to high-precision photometric time-series is challenging due to the wide point spread function (PSF) and the blending of stellar light in such dense regions. We developed an image-subtraction-based *K2* reduction pipeline that is applicable to both crowded and sparse stellar fields. We applied our pipeline to the data-rich C0 *K2* super-stamp, containing the two open clusters, as well as to the neighboring postage stamps. In this paper, we present our image subtraction reduction pipeline and demonstrate that this technique achieves ultra-high photometric precision for sources in the C0 super-stamp. We extract the raw light curves of 3960 stars taken from the UCAC4 and EPIC catalogs and de-trend them for systematic effects. We compare our photometric results with the prior reductions published in the literature. For detrended, TFA-corrected sources in the 12–12.25 K_p magnitude range, we achieve a best 6.5 hour window running rms of 35 ppm, falling to 100 ppm for fainter stars in the 14–14.25 K_p magnitude range. For stars with $K_p > 14$, our detrended and 6.5 hour binned light curves achieve the highest photometric precision. Moreover, all our TFA-corrected sources have higher precision on all timescales investigated. This work represents the first published image subtraction analysis of a *K2* super-stamp. This method will be particularly useful for analyzing the Galactic bulge observations carried out during *K2* campaign 9. The raw light curves and the final results of our detrending processes are publicly available at <http://k2.hatsurveys.org/archive/>.

Subject headings: open clusters and associations: individual (M35), (NGC 2158) — stars: variables: general — methods: data analysis — techniques: image processing, photometric -surveys -astrometry / *K2*

1. INTRODUCTION

Since its launch in April of 2008, the *Kepler Space Telescope* has systematically detected an unprecedented number of exoplanet candidates from the photometric signatures that these sources impart as they transit their host stars (e.g. Mullally et al. (2015)). Undoubtedly, the *Kepler* mission has played a pivotal role in the field of exoplanetary science, contributing the largest catalog of exoplanet candidates to date: 2/3rd of the current exoplanetary census data (Morton et al. 2016).

The *Kepler* photometer is a single-purpose instrument with a 0.95-m aperture Schmidt telescope design and a wide, ~ 100 -square-degree field of view (FOV). A detailed description of the *Kepler* mission can be found in Borucki et al. (2010) and Koch et al. (2010). During the primary phase of the *Kepler* mission, the spacecraft pointed toward a single patch of sky, simultaneously observing more than 100,000 stars.

In 2013, after four years of service, it was necessary to revise the direction of the mission after the failure of the second gyroscopic reaction wheel, a requisite to maintain telescope pointing stability. This event ushered in the second phase of the mission, the *K2 Ecliptic Survey*

(*K2*), designed to exploit the solar radiation and firing of thrusters as a means of maintaining pointing precision (Howell et al. 2014). *K2* operations started in June of 2014. Remarkably, aside from the failure of the two reaction wheels, the *Kepler* spacecraft exhibits little performance degradation and fuel budget estimates suggest a duration of 2–3 years for this second phase.

K2 observes a series of target fields, known as campaigns, along the plane of the ecliptic, for a span of ~ 75 days each. Through the numerous pointings scanning a multitude of Galactic coordinates, the *K2* mission provides a novel opportunity to probe transiting planets among diverse stellar populations. Each individual campaign targets $\sim 10,000$ – $20,000$ stars to be observed at 29-min cadence, as well as an additional ~ 100 targets that are observed at 1-min cadence. Observations are also made for a number of open and globular clusters, including M35, NGC 2158, M4, M80, M45, NGC 1647, the Hyades, M44, M67, and NGC 6717. The data are made publicly available in a series of data releases. To date, Campaigns 0–8 have been publicly released and are available on NASA’s Barbara A. Mikulski Archive for Space Telescopes (MAST).

Our campaign of interest, C0, is the first target field, observed during March–May 2014, and pointed toward the dense Galactic anti-center. Approximately 22,000 targets were observed in C0. Additionally, the open clusters M35 (NGC 2168) and NGC 2158 were observed during this campaign in what is known as a *super-stamp* — a contiguous aggregate of 154 separate postage stamps (50×50 pixels each) placed over the densest region of

¹ Department of Astrophysical Sciences, Princeton University, Princeton, NJ 08544, USA; email: msoares@astro.princeton.edu

[†] National Science Foundation Graduate Research Fellow

* Alfred P. Sloan Research Fellow

** Packard Fellow

² Astrophysics Department, Dunlap Institute for Astronomy and Astrophysics, University of Toronto, Toronto, ON M5S 3H4, Canada

these neighboring clusters. The open cluster M35 is at a distance of 762 ± 145 pc and has an estimated age of 150 Myr (McNamara et al. 2011). It is relatively sparse compared to NGC 2158, which is at 3600 ± 400 pc, and 2 Gyr old (Carraro et al. 2002). NGC 2158 is very dense, and was once believed to be a globular cluster.

Open clusters offer an invaluable opportunity to probe stellar and planetary astrophysics given the availability of cluster parameter constraints (e.g. age, metallicity, Galactic position and motion), as well as parameters for stellar members (e.g. stellar mass and evolutionary state). Moreover, the age of M35 makes it an ideal environment to study planetary evolution, as planets are known to undergo rapid evolutionary changes during the first few hundred million years after their formation (Adams & Laughlin 2006). To date, only a handful of candidate exoplanets have been found in open clusters, primarily through radial velocity measurements (e.g. Sato et al. (2007); Lovis & Mayor (2007); Quinn et al. (2012); Libralato et al. (2016b)). Using the *Kepler* satellite, Meibom et al. (2013) unveiled the first transiting exoplanet detection in an open cluster. More recently, data from the *K2* mission has continued to reveal transiting exoplanets in open cluster environments (Libralato et al. 2016b; Mann et al. 2016b,a). There remains much to be learned regarding this intriguing class of objects, such as whether exoplanets are a ubiquitous presence in dense open cluster environments.

In crowded open cluster fields, however, heavy blending of light from neighboring stars is unavoidable. This problem is only amplified by the large pixel size, wide PSF, and the lower pointing stability of the *K2* mission. As a result, simple aperture photometry is not an optimal means of obtaining high-precision stellar photometry. Our work aims to fully exploit the data-rich *K2* super-stamps using an image subtraction reduction technique, also known as “differential image analysis,” outlined by Alard & Lupton (1998). We fully automate this procedure into a reduction pipeline and apply it to sources in the C0 super-stamp.

There have been numerous investigations focusing on the same data set in the past. Vanderburg (2014) derived photometry for C0 data using an efficient detrending correction technique outlined in Vanderburg & Johnson (2014). This work focused solely on proposed *Kepler* target postage stamps, omitting cluster members and neighboring stars located on the C0 super-stamp. The first variability search on C0 target postage stamps was performed by Armstrong et al. (2015), also excluding the C0 super-stamp. This culminated in the identification of 8395 variable sources.

The first photometric results for C0 cluster members were obtained by (Libralato et al. (2016a), hereafter L16), curtailing the adverse effects of light blending by employing a well-established PSF neighbor-subtraction method, known to be an effective tool for extracting high-quality time series data in dense fields, and then performing aperture photometry (Montalto et al. 2007). They employ the high-angular-resolution Asiago Input Catalog (AIC), assembled from observations by the ground-based Asiago Schmidt Telescope. This catalog lists 75,935 objects in the region containing M35 and NGC 2158 (Nardiello et al. 2015). While the AIC extends to faint magnitudes of $K_p \simeq 24$, the rms scatter (defined as the

3.5σ -clipped 68.27th-percentile of the distribution about the median value of the light curve magnitude) for such dim stars is on the order of 50 times greater than that of sources in the 10–11 magnitude range. Moreover, as our primary aim is to search for planetary transits in dense *K2* fields, we focus our sources for which reasonable photometry can be retrieved ($\text{rms} < 0.02$).

The PSF neighbor-subtraction method requires high accuracy in the PSF modeling, otherwise the technique will produce false residuals and systematic errors — a concern that our image subtraction technique circumvents. The work of L16 resulted in a catalog of 2,133 variable stars found within the C0 super-stamp.

Our work provides the first image subtraction reduction of the C0 super-stamp, effectively removing sources with no detectable variability from the cluster field, therefore reducing blending, to produce high-precision differential photometry. While applying the image subtraction reduction technique to *K2* super-stamps is novel, the method itself is not a new concept. Alard & Lupton (1998) outlined this procedure nearly two decades ago, releasing the ISIS package and then further optimizing this process by incorporating a space-varying convolution kernel (Alard 2000). We make use of the image subtraction implementation of the HATNet project (Bakos et al. 2010) as described by Pál (2012).

The crowding from variable sources and the photon-noise residuals of non-variable sources on the image-subtracted frames is much smaller than crowding present on the original unsubtracted frames. This is because the vast majority of photometric sources tend to be either not detectably variable or they are only variable over long timescales. The image subtraction technique therefore offers the major advantage of far less blending in the resulting photometry. Furthermore, rather than modeling each of the images for a given cadence, we model the *changes* between images, which include variations in pointing, flux scaling, background, and the convolution kernel relating PSFs. These variations tend to be simpler to accurately model and are generally well fit by simple functions. The PSF, background, star positions, and relative fluxes are determined only once for a single photometric reference frame, which, in our case, is the median valued co-added frame taken from the entirety of our selected data set. Moreover, systematic errors that arise produce an increase in the overall amplitude of a light curve (a scaling error), rather than contributing to light curve noise. In contrast, proper modeling of the non-subtracted frames requires accurate modeling of the PSF, positions, background, and relative fluxes, which is far more challenging, particularly for an open cluster region where blending is profuse. One additional advantage of the image subtraction is that the source of the variation is often uniquely identified from the excess (or missing) residual flux at a given location, even under strong crowding.

In this paper, we reduce data from the *K2* C0 super-stamps and neighboring target pixel files to produce high-precision photometry for sources down to $K_p \sim 16$, employing techniques developed from the HAT ground-based transit surveys (Bakos et al. 2010) and building upon the work of Huang et al. (2015). We publicly release the raw and detrended high-precision light curves. We briefly review *K2* observations and describe C0 data

extraction in Section 2. The data reduction method is reviewed in Section 3, including astrometry, image subtraction, and photometry. Our detrending techniques are discussed in Section 4. Finally, in Section 5, we compare our C0 photometry and light curves with those obtained from prior studies (specifically that of L16), and demonstrate that we have generated the most precise photometric analysis of sources in C0 super-stamp. This is followed by a summary of our current efforts to conduct a variability search of our time series data.

2. OBSERVATIONS

2.1. *K2* Data Acquisition

A thorough review of the *Kepler* instrument is given in *The Kepler Instrument Handbook* (2009). Here we summarize the principal features of *K2* data acquisition.

The *K2* photometer is comprised of a 21-module array covering 5-square-degrees on the sky, providing ~ 100 -square-degree FOV. Each module contains two separate 2200×1024 pixel CCDs for a total of ~ 95 million pixels across the array. Two of the 21 modules were not operable when these observations were made and, more recently, a third module has also failed. Each module contains 4 output channels, designated by channel numbers 1–84. To prevent saturation, CCDs are read out every six seconds and the data are integrated for either a *long* 29-minute cadence or a 1-minute *short* cadence. To improve the photometric precision, images are de-focused to produce 10 arc-second wide PSFs.

In the *K2* phase the spacecraft is pointed toward the ecliptic in order to minimize the impact of solar radiation pressure. The still functioning two reaction wheels respond to the pressure exerted by solar radiation, providing a close to constant pointing alignment in the y and z axes, while the thrusters are fired to correct for drift along the x-axis every ~ 6 hours.

The coordinates of target sources in the *K2* mission are provided by the Ecliptic Plane Input Catalog (EPIC). The number of target objects is limited by the onboard storage, compression, and downlink capabilities, as well as the duration of the campaign. Observations of each target source, also known as a *Kepler Object of Interest* or *KOI*, are downloaded once per month as a 25×25 pixel postage stamp centered on the target, comprising 10% of the entire *Kepler* field — although some postage stamps can be as large as 50-pixels across. super-stamps are assigned a custom aperture number to serve as an identifier. Also obtained are two Full Frame Images (FFI) at the start and end of each campaign.

2.2. *K2* C0 Data Extraction

Our region of interest is the C0 super-stamp containing the open clusters M35 and NGC 2158, comprised of 385,000 individual pixels. These data are found on a single module output channel — channel 81. We make use of the *long*, 29-min cadence observations. Our data were obtained as target pixel files (TPFs) from NASA’s Barbara A. Mikulski Archive for Space Telescopes (MAST). TPFs are the time series pixel data for a particular stamp, centered on a target object. Unfortunately, the first half of the C0 observations were conducted in coarse pointing mode, resulting in large positional variations by up to ~ 20 pixels ($25 \text{ mas pixel}^{-1}$). Therefore, we solely analyze

the second half of the data set, which has a baseline of ~ 31 days (1840 cadences), where fine pointing mode was employed and the positional variations are significantly diminished. In contrast, the light curves generated by L16 employ the full data set.

3. DATA REDUCTION

The data reduction process employed for our image subtraction pipeline is based on the procedures described by Huang et al. (2015). Here we give a brief outline, and then discuss the process in more detail:

1. For each cadence, we employ header information from the TPFs to generate a sparse frame image, which contains all sources observed on the *K2* super-stamp and adjacent stamps.
2. We perform source extraction on the stars present in the *K2* super-stamp and adjacent TPFs and find an absolute astrometric transformation between the UCAC4 catalog (RA and Dec) and the extracted (x, y) positions of the sources in the frame.
3. An astrometric reference frame is selected. We use a sharp sparse frame image with median directional pointing.
4. We then spatially transform all sparse frame images to a common astrometric reference coordinate frame. This is accomplished by finding a transformation between the pixel coordinates of source centroids in a particular sparse frame image and the selected astrometric reference frame. This is a crucial step, minimizing the effect of spacecraft drift and allowing for more accurate modeling of the motion of the instrument in our detrending analysis.
5. We generate a master photometric reference frame, which is a stacked median average of all available C0 frames, after transforming to a common astrometric frame and matching their backgrounds and PSFs.
6. Each sparse frame cadence file is matched to and then subtracted from the photometric reference frame, leaving behind subtracted images showing only the variability in the field.
7. We perform photometry on the catalog projected sources (using the absolute astrometry above).
8. We then assemble light curves for all of the sources.
9. We apply a high-pass filter to our data (using 1-day binning) and perform a parameter decorrelation procedure, analogous to that outlined by Vanderburg & Johnson (2014), to remove the remaining small, time-correlated noise from our light curves.
10. We then apply the *Trend Filtering Algorithm*. (Kovács et al. 2005), as implemented in VARTOOLS (Hartman & Bakos 2016) to further remove systematic artifacts from the data.

3.1. Source Catalog Preparation

Our astrometry procedure is dependent upon an independent knowledge of the true positions of the observed celestial sources. For this, we employ the fourth edition of the United States Naval Observatory CCD Astrograph Catalog (UCAC4) (Zacharias et al. 2013). This catalog is based upon observations with a much higher spatial resolution than the *K2* observations and, as such, provides more accurate positions and photometric measurements than what can be deduced from the data alone. UCAC4 covers a stellar brightness range of 8th-16th magnitude in a single bandpass between V and R. Positional errors are on the order of 15–20 mas for stars in the range 10th-14th magnitude. Measurements are based on the International Celestial Reference System (ICRS) at a mean epoch of 2000. In addition to positional coordinates, the UCAC4 lists measurements of proper motion for $\sim 92\%$ of cataloged stars with errors on the order of 1–10 mas yr $^{-1}$. In the work performed by Huang et al. (2015), first-order corrections were applied to the coordinates of catalog objects based upon the proper motions to account for positional changes.

These catalogs are imperative to determining accurate brightness measurements for sources, as they have high spatial resolution, and are therefore less impacted by blending. The UCAC4 is supplemented by photometric data from the Two Micron All Sky Survey (2MASS) (Skrutskie et al. 2006) for $\sim 92\%$ of cataloged stars (J, H and K bands), as well from the AAVSO Photometric All-Sky Survey (APASS) for $\sim 45\%$ of objects (BVgri bands).

The *Kepler* magnitude (K_p), a measure of the source intensity as observed through the wide *Kepler* bandpass, is computed for all sources using pre-existing photometric data. Following the hierarchical conversion method outlined in Brown et al. (2011), we employ *gri* band photometry whenever possible. For sources without these measurements, however, we employ *BV* band magnitudes from the Tycho-2 catalog (Høg et al. 2000). For a subset of sources, we use B and V magnitude measurements to estimate *Kepler* magnitudes.

In addition to the *K2* target sources, our astrometric analysis provides positions and photometry for many other stars falling on the super-stamp and adjacent target pixel files. In total, 120 of our final light curves are *K2* target sources, while the remaining 3840 light curves are for objects that are not targeted *K2* sources.

3.2. Image Preparation and Astrometry

3.2.1. Sparse Frame Image Construction

We make use of the publicly available *K2* C0 TPFs, generating a sparse frame image of the entire channel for each cadence by stitching together the individual target pixel stamps. This is a useful alternative to working with a multitude of separate target pixel stamps. We use the available fits header information to determine the proper placement of target pixel stamps and compare our results with the FFI for that same field.

Each sparse frame image is comprised of a field of 1132×1070 square pixels, and unobserved regions in the sparse frame image are masked. A *Python* script automates the translation and stitching procedure, reconstructing a total of 1,392 high-quality sparse frame im-

ages in fine-pointing mode, with each image corresponding to an individual cadence. These frames are cross-checked with the FFI to ensure proper reconstruction. Figure 1 shows one example of a sparse frame image.

3.2.2. Relative Astrometry

The next step is a translation of each of the cadence frames into a common reference coordinate system. The astrometric reference file is a sparse frame image that sets the coordinate reference frame. The astrometric reference file is selected for its sharp stellar profiles, as compared to the other files, and a pointing position that is close to the median pointing over the duration of the observations.

We perform source extraction on the astrometric reference frame. We use the tool *fistar*, available in the astronomical image and data processing open-source software package *FITSH*, to detect and extract sources from the images. The *fistar* tool designates source candidate pixel groups, modeled in our case by an asymmetric Gaussian profile in order to derive precise centroid coordinates and shape parameters. We then extract the PSF for the image, based on the modeled sources. The output file is a list of detected and extracted sources (e.g. positions, S/N, Flux).

We then employ the *FITSH* tool *grmatch* to match detected sources from each of the sparse frame images to that of the astrometric reference frame. Matching is performed using a 2-dimensional point matching algorithm, determining an appropriate geometrical transformation to transform the points from each sparse frame cadence image to the astrometric reference frame, finding as many pairs as possible (Pál & Bakos 2006).

The output file contains the relevant geometrical transformation and statistics regarding the quality of the transformation. We employ an adapted version of the *FITSH* tool *fitrans* to perform the appropriate geometric transformations on each of the sparse frame cadence files. We use linear interpolation between the pixels involving exact flux conservation by integrating on the image surface.

The relative astrometry step is vital as it (a) generates accurate centroids for sources and (b) mitigates negative effects introduced by the spacecraft roll, which allows for more accurate modeling of the instrument motion in our detrending procedure. The original *Kepler* mission was known for its excellent pointing stability, while *K2* observations are plagued by significant pixel drift, with a typical star shifting along a ~ 2 -pixel long arc in our C0 data set. Variations in the pixel sensitivity produce fluctuations in the measured flux as a function of centroid position. Not surprisingly, the resulting PSF is distorted and blending is recurrently inevitable, particularly in dense stellar regions. Determining an accurate PSF shape is a crucial step in obtaining high-precision photometry in crowded fields like C0.

3.3. Image Subtraction

For *Kepler* and *K2*, aperture photometry is the primary method employed to derive light curves. Certain regions, however, are crowded, partly due to *Kepler's* large, undersampled pixels (~ 4 arcsec/pixel). Moreover, the PSF extends across several pixels. Here aperture

photometry can perform sub-optimally. Subtracting out the flux from non-varying sources is a means of teasing out the photometric variable sources in crowded regions L16 used the high-resolution AIC (Asiago Input Catalog) to identify neighbors for sources in the C0 super-stamp field, subtracting out the contributions from these contaminants.

Our method, however, instead relies on the creation of a stacked frame, coined the *photo-reference frame*, comprised of all 2419 K2 C0 frames. We explored multiple methods to generate the optimal photo-reference frame by varying the number of frames in the stack, employing quality cuts on frames included in the stack, and trying different averaging techniques. After comparing the resulting light curve quality and rms scatter of these routes, we conclude that the optimal photo-reference frame is generated by astrometrically matching our sparse frame images with `fitrans`, convolving the set of frames to match their corresponding PSFs and backgrounds, and then combining them to take the mean flux. We use the `ficonv` tool from the FITSH package to match and convolve the frames. We note that matching the backgrounds is particularly important due to the considerable changes in the zodiacal background light over the campaign.

After generating the photo-reference frame, we then use `ficonv` to match the background and PSF of each stitched frame cadence image to that of the photo-reference image before subtracting the two frames from one another. In order to properly do this we optimize the selected convolution kernel parameters, settling on a discrete image subtraction kernel over a Gaussian kernel.

With the frames appropriately convolved, we subtract photo-reference frame from each of the convolved individual cadences, leaving behind a sparser stellar field of varying sources (and residuals left after constant stars), as shown in Figure 1.

In addition to reducing blending in crowded regions, image subtraction affords the ability to uniquely identify sources from the excess (or missing) residual flux at a given location, even in dense stellar fields.

3.3.1. Image Subtraction Kernel

We parameterize the transformation that matches an observed image to the photo-reference image using a model of the form:

$$\begin{aligned}
 I'_{ij} = & \sum_{l=0}^{l=O_B-m} \sum_{m=0}^{m=O_B} b_{lm} i^l j^m \\
 & + \sum_{l=0}^{l=O_I-m} \sum_{m=0}^{m=O_I} K_{00lm} i^l j^m \times I_{ij} \\
 & + \sum_{l=0}^{l=O_K-m} \sum_{m=0}^{m=O_K} \sum_{i',j'=-k, i'j' \neq 00}^{i',j'=k} K_{i'j'lm} i^l j^m \\
 & \times (I_{i+i',j+j'} - I_{ij})/2,
 \end{aligned}$$

where I_{ij} represents the image undergoing analysis, I'_{ij} is the corresponding transformed image. The free parameters b_{lm} signify changes in the background, K_{00lm} signify changes in the flux scaling, and $K_{i'j'lm}$, with $i'j' \neq 00$, represent the discrete convolution kernel mod-

eling changes in the shape of the PSF. We use polynomials in the spatial coordinates (i, j) to represent spatial variations in each of these transformations. The order of the polynomial is given by O_B , O_I and O_K for the background, flux scaling, and PSF shape changes, respectively. The free parameters are linearly optimized to minimize the sum

$$\sum_{ij} (I'_{ij} - R_{ij})^2,$$

where R represents the photo-reference image. We explored a variety of values for the half-size of the discrete convolution kernel (k), and the spatial polynomial orders O_B , O_I and O_K . We settled on the optimal value of $k = 2$. We also found that assuming no spatial variation in the parameters ($O_B = O_I = O_K = 0$) generally provided the best results.

The optimal kernel parameters for each source are listed in the final column in Table 2 in the format “b0i0d20” (the numbers here represent example discrete kernel values that produces high-quality results). The number following ‘b’ represents the optimal value of O_B for that source. The value following ‘i’ sets O_I . The two numbers following ‘d’ represent k and O_K , respectively. For all sources we find that the light curve scatter is minimized when adopting $O_I = O_K = 0$ and $k = 2$. The optimal value for the order of the constant offset background kernel O_B , however, varies on a source-by-source basis, ranging between 0–4.

3.4. Photometry

There are two steps in performing photometry using subtracted images: 1. measuring the total fluxes of each of the sources on the photo-reference image, and 2. measuring the differential fluxes of each of the sources on each of the subtracted images. The total flux of a given source on a given image is then the sum of the reference flux of the source and the differential flux of the source for the image in question.

Determining the reference fluxes in this case is complicated due to the low spatial resolution of K2 and the significant blending of sources in the field of these clusters. We therefore make use of the UCAC4 determined K2 magnitudes, which are based on higher spatial resolution images, to set the relative fluxes of all sources in the field. To determine the zero-point flux level for the photo-reference image, we perform aperture photometry on the image using the `fiphot` tool in the FITSH package, and then determine the median ratio of the aperture photometry flux to the UCAC4 determined flux for unblended sources. Note that we are assuming in this process that none of the sources have varied in brightness between the UCAC4 and the photo-reference image, any violation of this assumption will lead to an error in the amplitude of variations in our image subtraction light curve, but will not distort the signal or add noise to it.

Differential fluxes are also computed using `fiphot`. We perform aperture photometry on the subtracted images at the fixed locations of the UCAC4 sources transformed to the image coordinates based on our astrometric solutions determined in Section 3.2. In order to ensure that the differential photometry is measured on a consistent system, `fiphot` makes use of the kernel parameters determined by `ficonv` to account for any changes in the

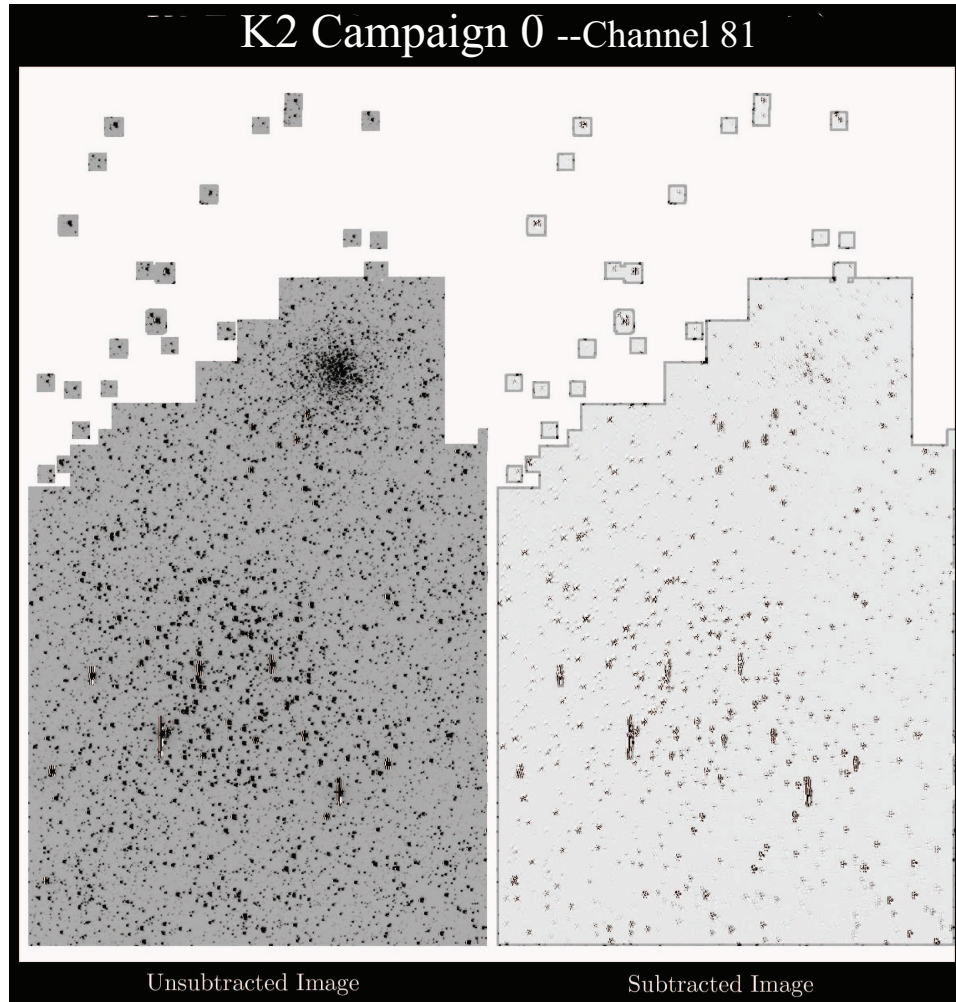


FIG. 1.— *K2* Campaign 0 super-stamp containing open clusters M35 and NGC 2158. The figure is generated by stitching stamps within a given channel (channel 81 in this case) into a composite image. The empty regions represent null pixels, as the information from these pixels are not downloaded by the spacecraft. The left panel displays the raw composite frame before our image subtraction reduction pipeline is applied. The right panel is an example of a single subtracted frame for an arbitrary cadence. Variable sources remain in the subtracted frame as well as bright stars that are still visible due to saturation or Poisson noise.

PSF shape or flux scale between the photo-reference and the subtracted image. We employ 9 apertures to measure the residual (differential) flux, ranging in size from 2.5 pixels to 5.0 pixels. The suggested optimal aperture for each source is then determined on a source-by-source basis, selecting the aperture with the lowest rms for each light curve.

4. LIGHT CURVE DETRENDING

While the image subtraction procedure should in principle correct for systematic variations in the images, leaving clean light curves free of instrumental variations, we found that, in practice, systematic variations remain, and post-processing is needed to remove these variations. As described in Section 2.1, the low frequency roll of the satellite causes sources to drift across the FOV. Thrusters are fired on timescales of ~ 6 hours to correct for this effect. This drift results in decreased photometric precision, as the star dithers between pixels changes in the pixel sensitivity must be taken into account. Fortunately this drift occurs largely along a single axis in a well defined motion, which greatly simplifies the necessary corrections.

There are several methods that have been employed to correct for systematic effects in *K2* data. These include a Gaussian process detrending approach outlined by Aigrain et al. (2015) as well as a method discussed in Foreman-Mackey et al. (2015), which performs simultaneous fit for systematics. We follow a procedure similar to the self flat-fielding detrending method outlined by Vanderburg & Johnson (2014), coined ‘K2SFF’, which corrects for drift systematics by decorrelating photometric light curves with the spacecraft motion.

The first step of our automated detrending procedure is a culling process whereby we remove all low-quality cadences. In the future, we plan to apply weights to each cadence rather than simply omitting a file from the data set. Our detrending method differs from that of Vanderburg & Johnson (2014) in that we do not rely on thruster flags labels as an indicator of file quality. Instead, we calculate the cadence-by-cadence drift between source centroids, clipping cadences where the drift exceeds 3.5σ . This method has an 82% overlap with thruster flagged cadences.

From this point, a median high-pass filter is applied to the culled data with binning windows of ~ 1 day.

Principal component analysis is then performed on the 2-dimensional scatter traced out by the source centroids as they drift with the spacecraft roll. This scatter is primarily 1-dimensional, and we therefore solely utilize the predominant basis vector. Corrections to account for changes in pixel response as a function of arclength offset (calculated as per Vanderburg & Johnson 2014) are applied. To apply the correction, we break up the predominant basis vector into 20 equally sized arclength offset bins, determining the median flux for each arclength bin. We then fit a B-spline function to the binned arclength offset vs. median flux curve.

The results of our detrending procedure can be seen in the light curves shown in Figure 2. This figure is discussed in greater detail in Section 5.

4.1. Trend Filtering Algorithm

In addition to the detrending process outlined above, we also include an optional post-processing step with the application of the Trend Filtering Algorithm (TFA), which is explained in detail in Kovács et al. (2005). We employ 141 TFA template stars, which are randomly chosen detrended light curve files containing more than 99% of all cadences.

The TFA technique, when applied in non-reconstructive mode as we do here, may not work well for long-period and/or high S/N variables. Instead of filtering out purely instrumental systematic variations or uncorrelated noise, the TFA will suppress and distort real variability from the source. For these high S/N and long period variables the non-TFA detrended light curves are optimal. The TFA does optimize our results for low S/N variables — where the signal is lower than the effect produced by instrumental systematics, as in this case the instrumental noise will be suppressed and the signal is more easily identified. If the magnitude variation is dominated by white noise, the TFA has negligible impact on the resulting light curve.

5. RESULTS AND DISCUSSION

In this paper we have presented our image subtraction technique to generate high-precision, detrended light curves for stars in the open clusters M35 and NGC 2158, observed in the Campaign 0 K2 field.

As L16 has already addressed a direct comparison between the neighbor-subtracted light curves and those generated in Vanderburg (2014), and since Vanderburg (2014) ignores the crowded super-stamp, we compare our results only with L16 to determine the robustness of the method.

Figure 2 compares our light curves to those of L16 for three representative variable sources identified by the L16 variable search. In general, the image subtraction light curves are comparable to those generated by L16 using neighbor subtraction, although in selected cases our precision is superior.

In addition to comparing individual sources, the top panel of Figure 3 shows the light curve rms scatter (at cadence) vs. *Kepler* magnitude for our pre-TFA detrended light curves, our post-TFA light curves, and the best aperture light curves from L16, to provide the reader with a sense of how these methods compare. The bottom panel shows the source-by-source ratio of the rms scatter of the L16 derived light curves our light curves

as a function of magnitude. For our detrended sources, 67.6% lie above the black Ratio = 1 line, and for our post-TFA sources 76.6% lie above this line, indicating a reduction in the light curve rms, which does not come at a cost to the signal amplitude.

In the top panel of Figure 4 we show the same results after binning the light curves by 6.5 hr, and in the third panel we show the results when computing the 6.5 hr running-window rms as defined by Vanderburg (2014) (this is computed to allow a more direct comparison to prior results, and is calculated by dividing the long-cadence light curves into bins of 13 consecutive cadences, computing the rms in each bin and dividing by $\sqrt{13}$, and then taking the median value over all bins). The second and fourth panels of Figure 4 display the source-by-source ratios (L16 to our data set) of the 6.5 hr binned rms and 6.5 hr running window rms (using only quality flagged data), respectively. We determine the ratios for both our detrended results and the TFA-corrected results.

We find that our pre-TFA detrended light curves are comparable to those of L16 (with a small improvement for fainter stars with $K_p > 14$ mag), while the post-TFA light curves have substantially less scatter on all timescales investigated. Part of this is due to the filtering by TFA of real stellar variability which is very common among the stars in these observations, however some of this is also due to the power of TFA at removing instrumental systematics. Figure 5 shows the median autocorrelation function of the light curves of bright sources with $11 < K_p < 12$. We find that while power at the 6 hr roll frequency is substantially reduced in the detrended light curve autocorrelation function, compared to what is seen for the raw light curves, there still remains a clear signature of these systematics even in the detrended light curves. This signal is completely removed in the TFA light curves, and the data are essentially uncorrelated in time.

For stars with $K_p > 14$ our detrended and 6.5 hour binned light curves achieve the highest precision to date for the C0 super-stamp. Post-processing of these light curves is still needed to remove systematics and search for small transiting planets. This work represents the first published image subtraction analysis of a K2 super-stamp. This method will provide a valuable means of analysis of the Galactic Bulge observations carried out during K2 campaign 9.

We make the subtracted images, raw light curves, and detrended light curves generated from the K2 C0 super-stamp publicly available at the HAT data server: <http://k2.hatsurveys.org/archive/>. The light curve files contain the following information: time of observation, cadence number, subtracted and detrended fluxes and associated errors for several apertures, raw relative fluxes and associated errors, centroid positions, and the accompanying PSF kernel parameters for our best resulting light curve. The format of the light curve files is given in Tables 1 and 2, for the detrended results (containing the data for the raw light curves therein) and the detrended with TFA light curves, respectively. Missing from Table 2 (in order to save space and omit redundancy) are the columns listing the raw and detrended rms values associated with all 9 possible apertures. We also

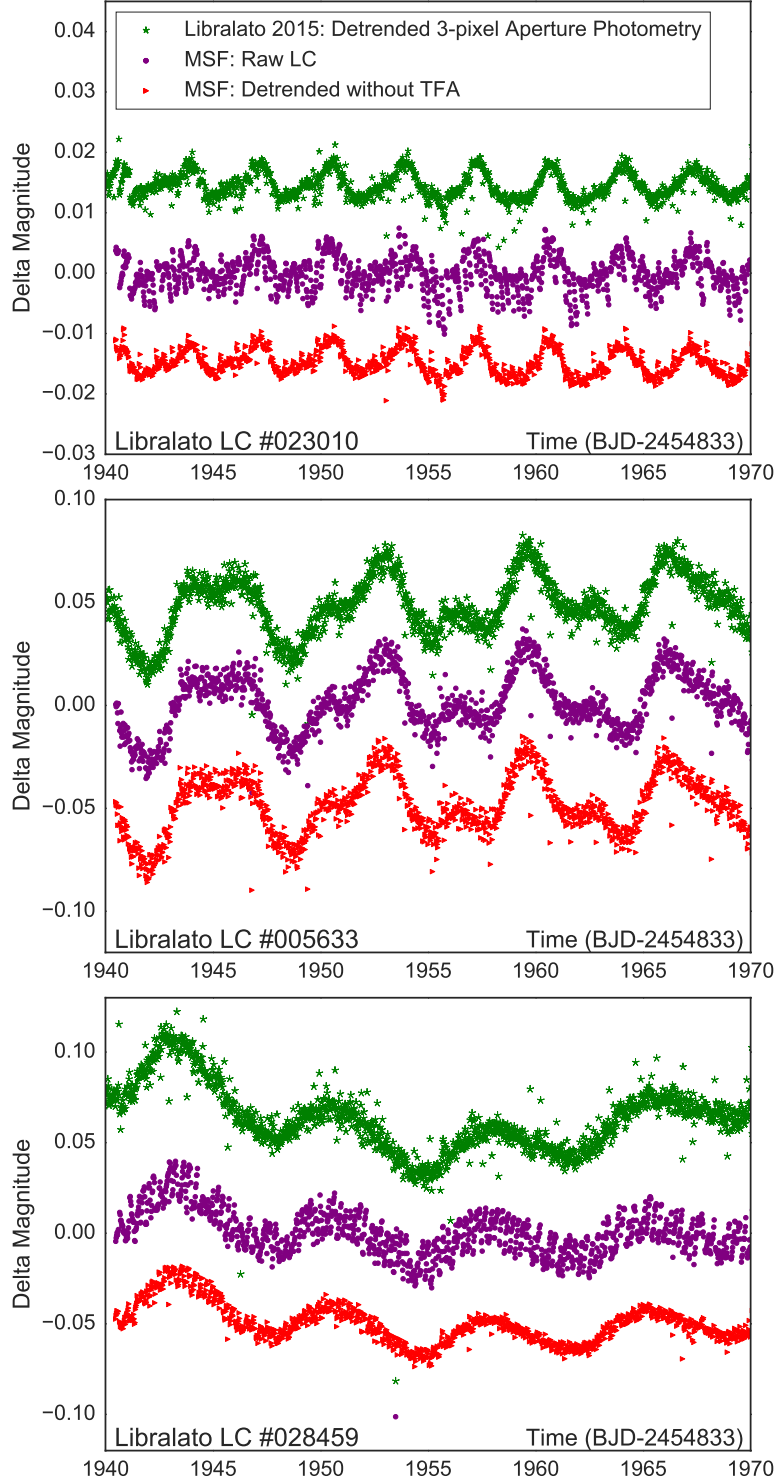


FIG. 2.— Direct comparison of our photometric results with known variable sources presented in L16. The *green, star-shaped points* illustrate the best aperture detrended results produced by L16 (these happen to be the detrended three-pixel aperture photometric results), while the *purple, round points* show our raw, image-subtracted, best aperture results for the same source. The *red, triangle-shaped points* display our detrended, best aperture photometric results without application of the TFA procedure. In both the top and middle panels, our results are comparable to that of L16, while in the bottom panel both our raw and detrended light curve show far less scatter.

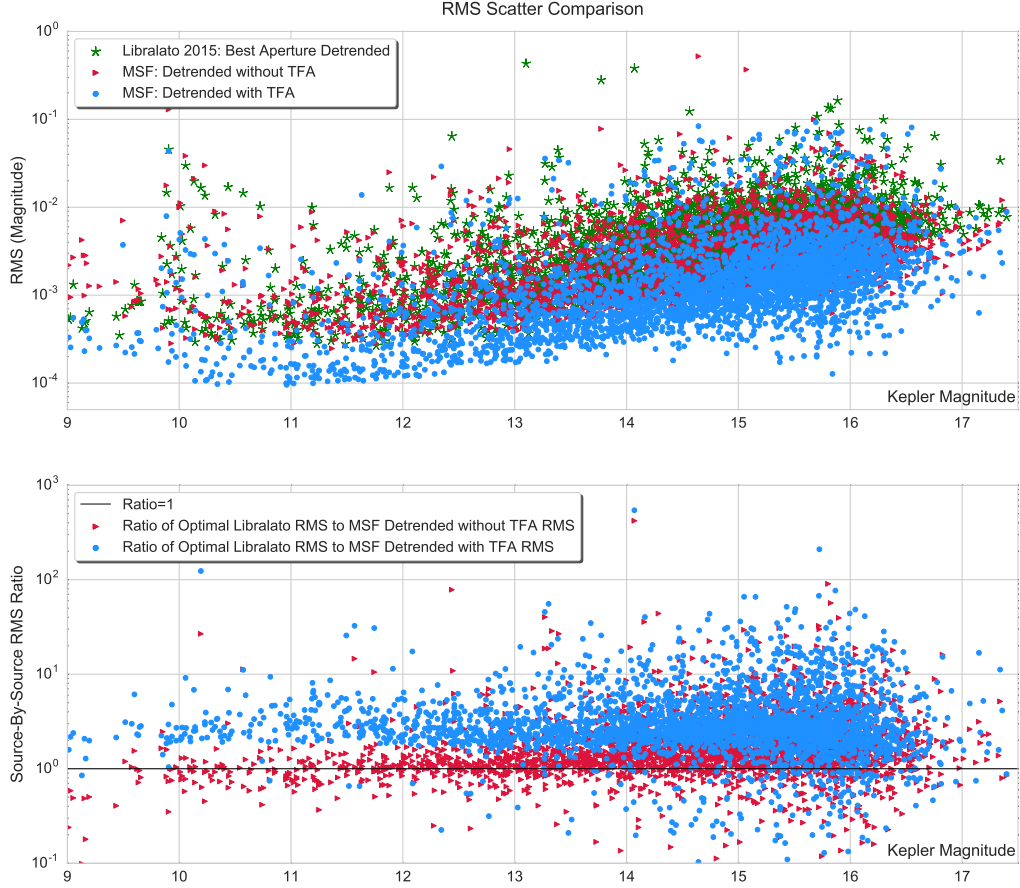


FIG. 3.— Direct comparison of the rms magnitude scatter of our detrended results to the best results produced by L16. In the top panel, we plot the rms magnitude versus Kepler magnitude for matching sources. L16 produced light curves for many more objects, especially faint sources with $K_p > 17$, but to provide a fair comparison of the precision of the two methods, we are only showing objects in these plots for which we also produced a light curve. The *green, star-shaped points* depict the L16 sources, while the *red, triangle-shaped points* display the rms magnitude scatter for our detrended light curves without the TFA application. The *blue, round points* show our rms magnitude scatter for TFA-corrected light curves. It is clear from the top panel that the TFA application reduces the rms considerably, however, not at a cost to the signal amplitude. Faint sources ($K_p \gtrsim 15$) with anomalously low rms are sources for which the catalog Kepler magnitude is brighter than the true magnitude on the photo-reference image, leading to underestimating the amplitude of photometric variations when computed in magnitudes. In the bottom panel we plot the source-by-source ratio of the L16 optimal rms magnitude scatter to that of our detrended rms (*red, triangle-shaped points*) and to that of TFA-corrected results (*blue, dashed points*). For our detrended sources, 67.6% lie above the *black line* where ratio = 1, and for our post-TFA sources 76.6% lie above this line.

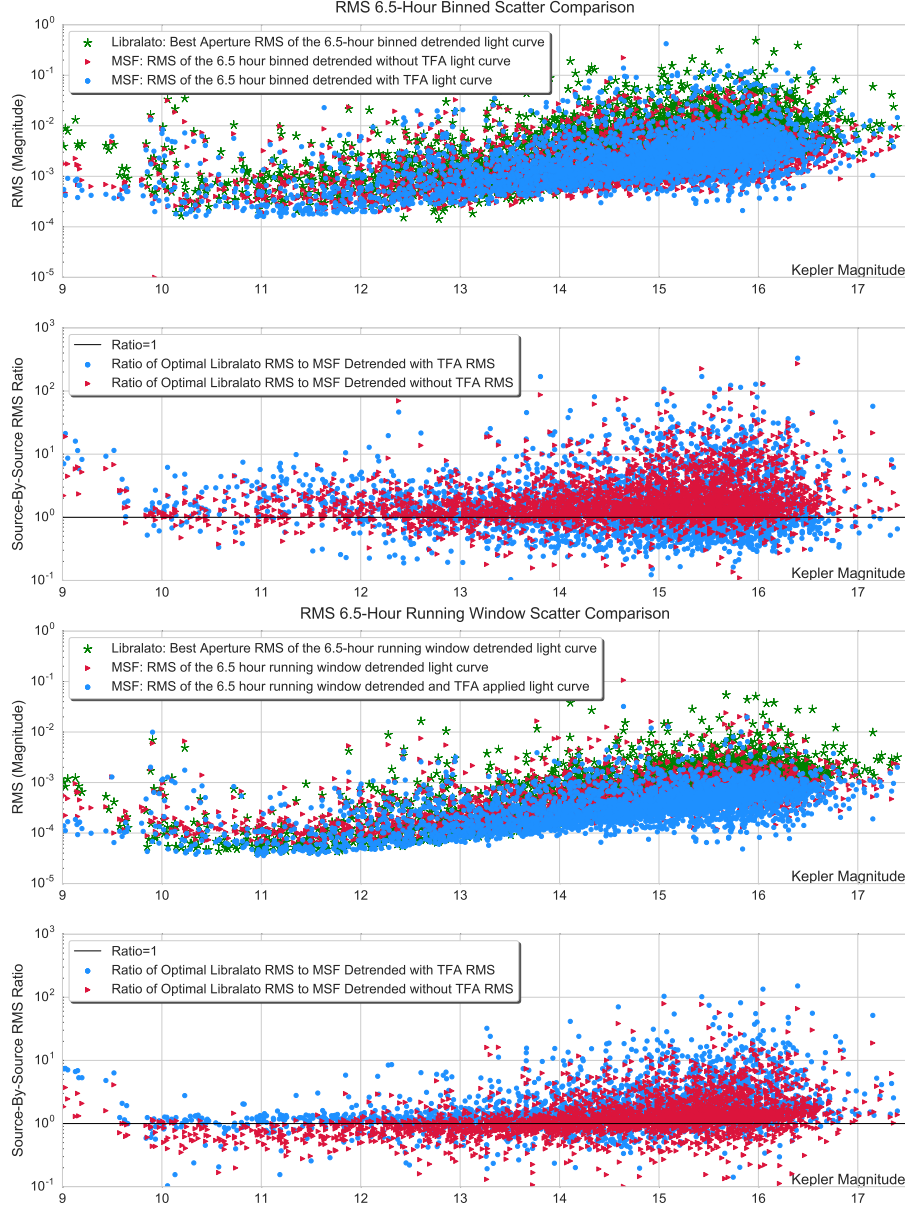


FIG. 4.— Direct comparison of the 6.5 hour binned rms magnitude scatter of our detrended and TFA-corrected results to the best L16 results in the top panel. The *green, star-shaped points* depict the 6.5 hour binned rms of the magnitude for all the L16 sources. The *red, triangle-shaped points* display our 6.5 binned rms magnitude scatter for detrended results without TFA, while the *blue, circle-shaped points* illustrate the magnitude scatter for results that are TFA-corrected. For a fair comparison, we do not show all L16 sources, and instead display only source matches between both data sets. The second panel from the top shows the source-by-source ratio of the L16 rms to our results for both the detrended results (*red, triangle-shaped points*) and the TFA-corrected results (*blue, round points*). The *solid black line* displays where ratio = 1. The third panel illustrates a comparison of the 6.5 hour running window rms magnitude scatter of our detrended and TFA-corrected results to that of L16. Once again, *green, star-shaped points* depict L16 sources, *red, triangle-shaped points* represent our detrended sources without TFA, and *blue, circle-shaped points* depict our TFA-corrected sources. In the bottom panel, we plot the source-by-source ratio of the L16 6.5 hour running window rms to our results for both the detrended results (*red, triangle-shaped points*) and the TFA-corrected results (*blue, round points*). The *solid black line* displays where ratio = 1. It is worth repeating that the reduced scatter in our light curves does not come at a cost of the signal amplitude.

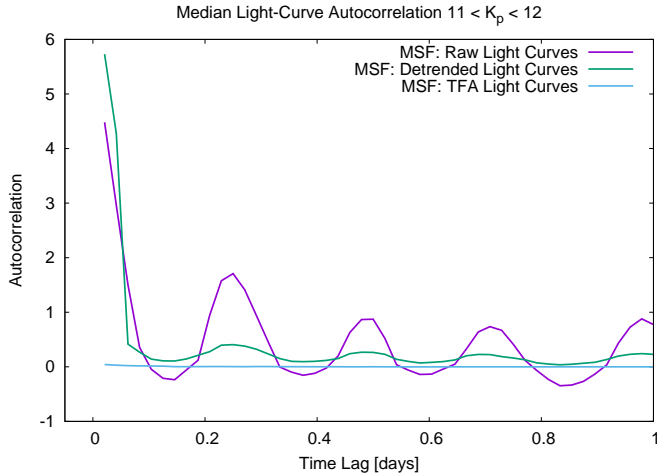


FIG. 5.— Median discrete autocorrelation function for sources with $11 < K_p < 12$, shown separately for our raw light curves, detrended light curves, and TFA-corrected light curves. The autocorrelation is computed relative to the formal photometric uncertainties. Values above unity indicate a co-variance exceeding the formal expected variance at zero lag. The raw light curves show clear periodicity at the 6 hr (0.25 day) spacecraft roll period. This periodicity is suppressed in the detrended light curves, but is still evident. The TFA light curves are effectively uncorrelated in time, and show no evidence for the 6 hr instrumental periodicity.

submit our results to the Barbara A. Mikulski Archive for Space Telescopes (MAST) to share them with the scientific community.

It is our hope that there will be continued improvements of the detrending methods and photometric analysis so that the C0 super-stamp may be exploited to its fullest potential, including searching the data for variable sources, which will be the subject of future work. In this paper we have taken the first step of demonstrating that the image subtraction method is capable of producing light curves from *K2* super-stamps with a precision that is comparable to that of the best method demonstrated to date. We note that L16 have independently detrended light curves and conducted a variable search on M35 and NGC 2158 cluster members resulting in a list of 2133 variables. For the clusters studied here we do not expect a significantly different yield of variables from our reduction as the light curves we have generated are of comparable precision to those of L16.

We are currently working on extending this pipeline to other crowded regions in the *K2* field, particularly Campaign 9, which points toward the dense Galactic Center. We also aim to apply the pipeline to searching for variables in globular clusters. It is likely that image subtraction will perform significantly better than the neighbor-subtraction method of L16 for these particularly crowded regions. *K2* observations have been made for a number of open and globular clusters, including M4, M80, M45, NGC 1647, the Hyades, M44, M67, and NGC 6717. We aim to fully exploit these data-rich fields using our image subtraction reduction pipeline in pursuit of new intrinsic variables and transiting planets.

Acknowledgments— MSF gratefully acknowledges the generous support from the National Science Foundation.

The data in this paper were collected by the *Kepler* mission, which is funded by the NASA Science

Mission directorate. The data were downloaded from the Barbara A. Mikulski Archive for Space Telescopes (MAST), a NASA-funded project providing astronomical data archives and stationed at Space Telescope Science Institute (STScI). STScI is operated by the Association of Universities for Research in Astronomy, Inc.

TABLE 1
DETRENDED + TFA LIGHT CURVE FORMAT

Cadence	Time Days: BJD-2454833	Detrended Best Ap Mag Normalized	Detrended Error Best Ap Mag	Raw Best Ap Mag	x-coord Image Coords	y-coord Image Coords	TFA Detrended Best Ap Mag Normalized
2200	1940.47759875	-0.00301	0.00813	13.96333	356.073	467.058	-0.0004
2201	1940.49803044	-0.00332	0.00813	13.96244	356.053	467.046	0.00025
2202	1940.51846192	-0.00279	0.00814	13.96163	356.017	467.038	0.00045
2203	1940.53889351	-0.00135	0.00814	13.96259	356.02	467.017	0.00227
2204	1940.5593252	0.00109	0.00813	13.96381	356.003	466.994	0.0018
2205	1940.57975669	-0.00941	0.00811	13.95302	355.987	466.985	-0.00864
2206	1940.60018828	0.00453	0.00815	13.96619	355.954	466.941	0.00154
2209	1940.66148304	0.0018	0.00817	13.9583	356.476	467.345	-0.0015
2210	1940.68191473	0.00349	0.00819	13.96045	356.454	467.354	-0.00051
2211	1940.70234632	0.00448	0.00821	13.96247	356.45	467.32	0.00134

TABLE 2
DETRENDED WITHOUT TFA LIGHT CURVE FORMAT

Time Days: BJD-2454833	Cadence	Detrended Best Ap Mag Normalized	Error Best Ap Mag	Raw Best Ap Mag	x-coord Image Coords	y-coord Image Coords	Arclength Param Image Coords	Optimal PSF Kernel b-i-d-
1940.4776	2200	-0.00301	0.00813	13.96333	356.073	467.058	0.6232	b0i0d20
1940.498	2201	-0.00332	0.00813	13.96244	356.053	467.046	0.6458	–
1940.5185	2202	-0.00279	0.00814	13.96163	356.017	467.038	0.6793	–
1940.5389	2203	-0.00135	0.00814	13.96259	356.02	467.017	0.6899	–
1940.5593	2204	0.00109	0.00813	13.96381	356.003	466.994	0.7174	–
1940.5798	2205	-0.00941	0.00811	13.95302	355.987	466.985	0.7355	–
1940.6002	2206	0.00453	0.00815	13.96619	355.954	466.941	0.7885	–
1940.6615	2209	0.0018	0.00817	13.9583	356.476	467.345	0.1287	–
1940.6819	2210	0.00349	0.00819	13.96045	356.454	467.354	0.1405	–
1940.7023	2211	0.00448	0.00821	13.96247	356.45	467.32	0.1638	–

REFERENCES

- Adams, F. C., & Laughlin, G. 2006, *ApJ*, 649, 1004
- Aigrain, S., Hodgkin, S. T., Irwin, M. J., Lewis, J. R., & Roberts, S. J. 2015, *MNRAS*, 447, 2880
- Alard, C. 2000, *A&AS*, 144, 363
- Alard, C., & Lupton, R. H. 1998, *ApJ*, 503, 325
- Armstrong, D. J., Kirk, J., Lam, K. W. F., et al. 2015, *A&A*, 579, A19
- Bakos, G. Á., Torres, G., Pál, A., et al. 2010, *ApJ*, 710, 1724
- Borucki, W. J., Koch, D., Basri, G., et al. 2010, *Science*, 327, 977
- Brown, T. M., Latham, D. W., Everett, M. E., & Esquerdo, G. A. 2011, *AJ*, 142, 112
- Carraro, G., Girardi, L., & Marigo, P. 2002, *MNRAS*, 332, 705
- Foreman-Mackey, D., Montet, B. T., Hogg, D. W., et al. 2015, *ApJ*, 806, 215
- Hartman, J. D., & Bakos, G. Á. 2016, *Astronomy and Computing*, 17, 1
- Høg, E., Fabricius, C., Makarov, V. V., et al. 2000, *A&A*, 355, L27
- Howell, S. B., Sobeck, C., Haas, M., et al. 2014, *PASP*, 126, 398
- Huang, C. X., Penev, K., Hartman, J. D., et al. 2015, *MNRAS*, 454, 4159
- Koch, D. G., Borucki, W. J., Basri, G., et al. 2010, *ApJ*, 713, L79
- Kovács, G., Bakos, G., & Noyes, R. W. 2005, *MNRAS*, 356, 557
- Libralato, M., Bedin, L. R., Nardiello, D., & Piotto, G. 2016a, *MNRAS*, 456, 1137
- Libralato, M., Nardiello, D., Bedin, L. R., et al. 2016b, *MNRAS*
- Lovis, C., & Mayor, M. 2007, *A&A*, 472, 657
- Mann, A. W., Gaidos, E., Vanderburg, A., et al. 2016a, *ArXiv e-prints*, 1609.00726
- Mann, A. W., Gaidos, E., Mace, G. N., et al. 2016b, *ApJ*, 818, 46
- McNamara, B. J., Harrison, T. E., McArthur, B. E., & Benedict, G. F. 2011, *AJ*, 142, 53
- Meibom, S., Torres, G., Fressin, F., et al. 2013, *Nature*, 499, 55
- Montalto, M., Piotto, G., Desidera, S., et al. 2007, *A&A*, 470, 1137
- Morton, T. D., Bryson, S. T., Coughlin, J. L., et al. 2016, *ApJ*, 822, 86
- Mullally, F., Coughlin, J. L., Thompson, S. E., et al. 2015, *ApJS*, 217, 31
- Nardiello, D., Bedin, L. R., Nascimbeni, V., et al. 2015, *MNRAS*, 447, 3536
- Pál, A. 2012, *MNRAS*, 421, 1825
- Pál, A., & Bakos, G. Á. 2006, *PASP*, 118, 1474
- Quinn, S. N., White, R. J., Latham, D. W., et al. 2012, *ApJ*, 756, L33
- Sato, B., Izumiura, H., Toyota, E., et al. 2007, *ApJ*, 661, 527
- Skrutskie, M. F., Cutri, R. M., Stiening, R., et al. 2006, *AJ*, 131, 1163
- van Cleve, J. E., & Caldwell, D. 2009, *Kepler Instrument Handbook*, Tech. Rep. KSCI-19033-001
- Vanderburg, A. 2014, *ArXiv e-prints*, 1412.1827
- Vanderburg, A., & Johnson, J. A. 2014, *PASP*, 126, 948
- Zacharias, N., Finch, C. T., Girard, T. M., et al. 2013, *AJ*, 145, 44